

# Decadal slowdown of a land-terminating sector of the Greenland Ice Sheet despite warming

Andrew J. Tedstone<sup>1</sup>, Peter W. Nienow<sup>1</sup>, Noel Gourmelen<sup>1</sup>, Amaury Dehecq<sup>1,2</sup>, Daniel Goldberg<sup>1</sup> & Edward Hanna<sup>3</sup>

**Ice flow along land-terminating margins of the Greenland Ice Sheet (GIS) varies considerably in response to fluctuating inputs of surface meltwater to the bed of the ice sheet. Such inputs lubricate the ice-bed interface, transiently speeding up the flow of ice<sup>1,2</sup>. Greater melting results in faster ice motion during summer, but slower motion over the subsequent winter, owing to the evolution of an efficient drainage system that enables water to drain from regions of the ice-sheet bed that have a high basal water pressure<sup>2,3</sup>. However, the impact of hydrodynamic coupling on ice motion over decadal timescales remains poorly constrained. Here we show that annual ice motion across an 8,000-km<sup>2</sup> land-terminating region of the west GIS margin, extending to 1,100 m above sea level, was 12% slower in 2007–14 compared with 1985–94, despite a 50% increase in surface meltwater production. Our findings suggest that, over these three decades, hydrodynamic coupling in this section of the ablation zone resulted in a net slowdown of ice motion (not a speed-up, as previously postulated<sup>1</sup>). Increases in meltwater production from projected climate warming may therefore further reduce the motion of land-terminating margins of the GIS. Our findings suggest that these sectors of the ice sheet are more resilient to the dynamic impacts of enhanced meltwater production than previously thought.**

The GIS is losing mass at an accelerating rate<sup>4,5</sup>, as a result both of increased surface melting<sup>6</sup> and of enhanced ice discharge from accelerating marine-terminating glaciers<sup>5</sup>. Enhanced melting accounts for about 60% of the GIS mass lost since 2000 (ref. 5); summer air temperatures over the southwest GIS warmed by 0.9 °C during 1994–2007 (ref. 7), and the amount of meltwater produced during the summers of 2007–12 (except 2009) is without precedent in the past 50 years of reanalysis-forced reconstructions<sup>8</sup>. During 1993–2012, the average annual melt doubled from that which occurred during 1961–90 (ref. 8).

While the acceleration of marine-terminating glaciers is believed to be driven primarily by processes operating at the ice–ocean interface, atmospheric forcing can also change ice motion at both land- and marine-terminating glaciers through the delivery of surface meltwater to the ice-sheet bed<sup>1,9</sup>. Surface meltwaters can drain rapidly to the ice-sheet bed via moulins and supraglacial lake drainage events, both of which provide direct surface-to-bed connectivity and a mechanism by which surface meltwater could influence basal motion<sup>10–12</sup>. It has been suggested that this mechanism could lead to a positive feedback between enhanced surface meltwater production and ice-sheet motion, as ice would move more quickly to lower elevations, where temperatures are warmer<sup>1,13</sup>.

Other studies have highlighted the importance of the subglacial drainage system in controlling the relationship between surface melting and ice motion through changes in system capacity and morphology<sup>14–16</sup>. During summer, rapid increases in meltwater from the ice-sheet surface result in periods in which the subglacial drainage system is more highly pressurized, leading to transient periods when the water pressure below exceeds the pressure caused by the weight of

the ice above, resulting in enhanced basal sliding<sup>15</sup>. However, the capacity of the subglacial drainage system then increases in response<sup>14,17</sup>, introducing a negative feedback that lowers the water pressure and reduces basal sliding<sup>16,18</sup>. By the end of summer, an efficient drainage system has evolved upglacier<sup>15,16</sup>, draining surrounding regions of the ice-sheet bed that were previously hydraulically isolated. This reduces basal lubrication during the subsequent winter, counteracting the summer speed-up and making net annual ice motion relatively insensitive to summer melting<sup>2,3</sup>.

Despite these advances in understanding the coupled hydrodynamics of ice-sheet flow, it remains unclear whether enhanced surface melting has a long-term impact on annual ice motion. Eight global positioning system (GPS) stations on a transect extending 130 km inland in the southwest GIS showed an average 10% decrease in ice flow from 1991 to 2007, during a period in which surface melt increased markedly, but there was considerable spatial variability<sup>19</sup>. The slowdown trend at lower sites continued into 2012 (ref. 20). Meanwhile, from 2009 to 2012 a small acceleration signal was observed above the altitude of the equilibrium line (where annual ice accumulation is equal to annual ablation), at ~1,500 metres above sea level (m.a.s.l.; ref. 21). The parametrization of basal lubrication in higher-order ice-sheet models, using observations from southwest Greenland, suggests that basal lubrication is unlikely to increase the contribution of the ice sheet to sea-level rise by more than 5% of the contribution that would be expected from a negative surface mass budget alone, and could conceivably act as a negative feedback upon ice motion<sup>22</sup>.

Here we present observations of annual GIS motion spanning three decades, which extend back to 1985. Our ~8,000-km<sup>2</sup> study area extends along about 170 km of the predominantly land-terminating margin of the west GIS, to ~50 km inland, and to ~1,100 m.a.s.l. (Fig. 1). We apply feature tracking (see Methods) to 475 pairs of remotely sensed optical Landsat images separated by approximately one year<sup>23</sup>. Next, we derive robust ice-motion and uncertainty estimates over periods of approximately one to two years from 1985 to 2014 (Fig. 2b and Extended Data Fig. 4), and over multiyear reference periods spanning, first 1985–94, capturing the period before air temperatures began to warm<sup>7</sup>; and second 2007–14, corresponding to the recent series of summers with record melting<sup>8</sup>.

Ice motion shows a clear regional slowdown (Fig. 1), with 84% of the study area flowing more slowly in 2007–14 than in 1985–94 (Fig. 1a). On average, ice motion slowed by 12% across the study area. Slowdown was strongest (~15–20%) at elevations below around 800 m.a.s.l. (Fig. 1b). Isolated areas experienced speed-up in 2007–14 compared with 1985–94. In the far northeast, the speed-up can probably be attributed to the dynamics of the neighbouring marine-terminating Jakobshavn Isbrae, which, like many of Greenland's marine-terminating glaciers, has accelerated since the mid-1990s (ref. 5).

We can divide the ice-motion record (Fig. 2b) into two statistically significant periods (see Methods). Segmented linear regression ( $R^2 = 0.79$ ) shows that there was no significant trend in ice motion during 1985–2002 ( $P = 0.85$ ). The slowdown in motion probably

<sup>1</sup>School of GeoSciences, University of Edinburgh, Edinburgh EH8 9XP, UK. <sup>2</sup>Université Savoie Mont-Blanc, Polytech Annecy-Chambéry, LISTIC, BP 80439, 74944 Annecy-le-Vieux cedex, France.

<sup>3</sup>Department of Geography, University of Sheffield, Sheffield S10 2TN, UK.

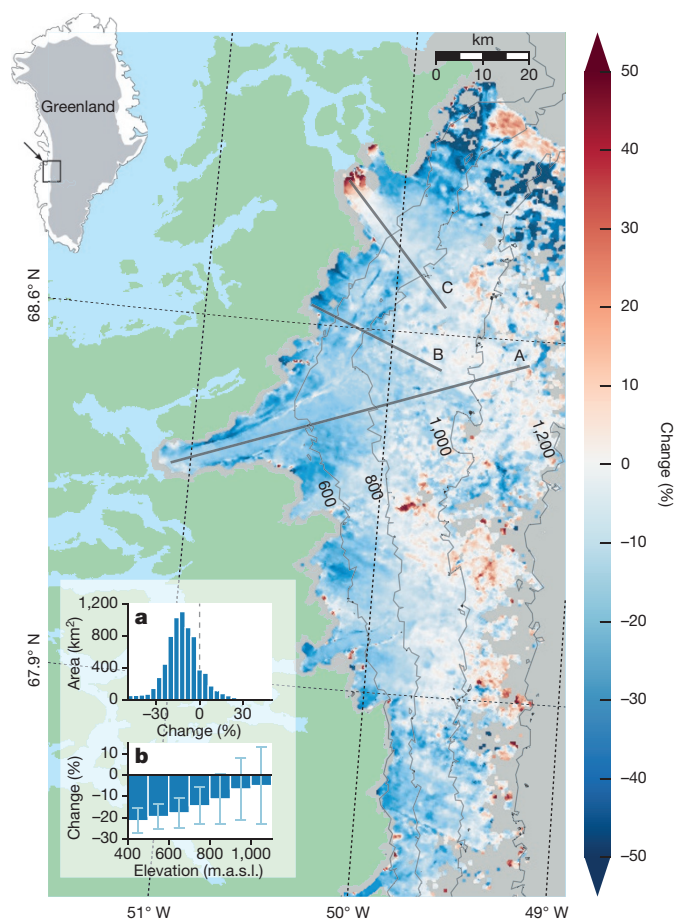


**Figure 1 | Study area in the ablation zone of the western GIS.** In the main figure, the colour scale shows the percentage change in ice velocities during the 2007–14 reference period compared with the 1985–94 reference period (see main text). Transects A, B and C correspond to data in Fig. 3. Ice surface contours (pale grey lines) are from ref. 30. Grey shading denotes areas where ice velocities cannot be resolved; green shading denotes land areas; light blue shading denotes inland and coastal waters. Inset: **a**, percentage changes in ice velocities in 4% bins; **b**, median percentage change in each 100-m elevation band between 400 m.a.s.l. and 1,100 m.a.s.l.,  $\pm 1\sigma$  (see Methods).

began around 2002, and, despite interannual variability, there was a robust overall trend of  $-1.5 \text{ m yr}^{-2}$  during 2002–14 ( $P < 0.01$ ). Meanwhile, we can divide surface meltwater production (Fig. 2a) into three statistically significant periods (see Methods): a sustained 'low' melt of 2.1 water equivalent (w.e.)  $\text{m yr}^{-1}$  during 1985–93; a rising melt during 1993–2002; and a sustained high melt of 3.2 w.e.  $\text{m yr}^{-1}$  during 2002–14, coincident with the slowdown in ice motion. Overall there was a 49.8% rise in surface meltwater production across our study area between 1985–94 and 2007–14.

We explored temporal variability in ice motion along three transects (Fig. 1), selected to represent different ice-marginal conditions. Transect A extends 80 km inland from the Nordenskjöld glacier, which has a lacustrine-terminating margin; transect B extends about 30 km inland from a land-terminating margin; and transect C extends about 30 km inland from the marine-terminating Alangordliup sermia. Transects A and B slowed down during 2000–14 to attain velocities, averaged along the transect, that were respectively 19% and 18% slower in 2013–14 than during 1985–94 (Fig. 3a, b). Ice-motion characteristics at the marine-terminating transect C were more complex (Fig. 3c). The transect slowed on average from the mid-2000s to 2014, although ice motion within 10 km of the margin sped up in the late 2000s following earlier slowdown, and by 2013–14 was flowing up to about  $50 \text{ m yr}^{-1}$  faster than during the 1985–94 reference period. Such behaviour is in line with other tidewater glaciers that have recently accelerated<sup>5</sup>.

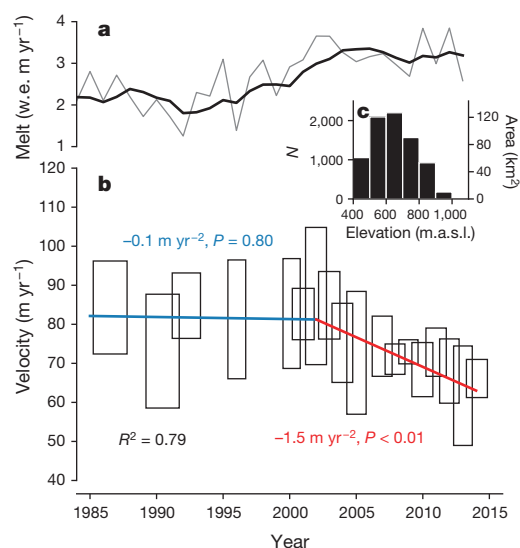


**Figure 2 | Surface melting and ice motion averaged over the study area.**

**a**, Annual mean modelled surface melt (grey), smoothed with a five-year moving mean (black), both in water equivalent (w.e.) m per year (see Methods). **b**, Median ice velocities during each period (black boxes) calculated using the common sampling pixels across the time series,  $\pm 1\sigma$  (see Methods). The width of each box corresponds to the total timespan of the pairs of Landsat images acquired during each period. The height of each box corresponds to  $\pm 1\sigma$  (see Methods). Blue and red lines illustrate the trends in ice velocity computed by segmented linear regression weighted by  $1\sigma$ . **c**, Altitudinal distribution of the common sampling pixels used to compute the velocities in **b**.

The slowdown signal across our predominantly land-terminating region extends up to about 1,100 m.a.s.l. (Fig. 1), where the mean ice thickness is roughly 850 m (ref. 24). The clear deceleration in ice motion requires a decrease in rates of either internal ice deformation, or basal motion, or both. Melting has caused marginal thinning of the GIS<sup>25–27</sup>. During 1993–98, land-terminating glaciers on the west GIS margin thinned by  $0.02\text{--}0.23 \text{ m yr}^{-1}$  below 1,000 m.a.s.l. (ref. 25). Our study area thinned by about  $0.2 \text{ m yr}^{-1}$  during 2003–07 (ref. 26) and this rate increased to  $1\text{--}1.5 \text{ m yr}^{-1}$  during 2011–14 (ref. 27). We modelled the velocity change that would be caused by 10–20 m of ice thinning (and the associated gradient changes) along transect A over the 1985–2014 study period (see Methods), corresponding to a maximum thinning rate of about  $0.6 \text{ m yr}^{-1}$ . The resulting change in driving stress can explain only around 17–33% of the observed overall 12% slowdown signal beyond 10 km from the ice-sheet margin, and can explain none of the slowdown beyond 50 km from the margin (Extended Data Fig. 5c). Thus, while a component of the observed slowdown can be explained by changes in driving stress through ice thinning, the majority of the slowdown (that is, the remaining 67–83%) must be the result of processes operating at the ice-bed interface that cause a reduction in basal motion.

Previous studies have suggested that the coupling between surface melting and basal motion is self-regulating, such that there is no statistically significant relationship between melting and ice motion over annual timescales<sup>2,20</sup>. In agreement with these studies, we find no relationship between annual melt volume and annual ice motion ( $R^2 = 0.08$ ). There is, however, a significant relationship between antecedent melt volumes and ice motion (Extended Data Table 1). The mean melt volume from each observation period and the previous year combined explain 23% of ice motion ( $P < 0.05$ ), increasing to 44% when the previous four years of melt are included. Moreover, melt volumes explain 50% of ice motion when the mean melt volume is calculated using only the previous three years' data ( $P < 0.01$ ).

We therefore suggest that sustained high production of surface meltwater (Fig. 2a) is responsible for the slowdown. Observations from

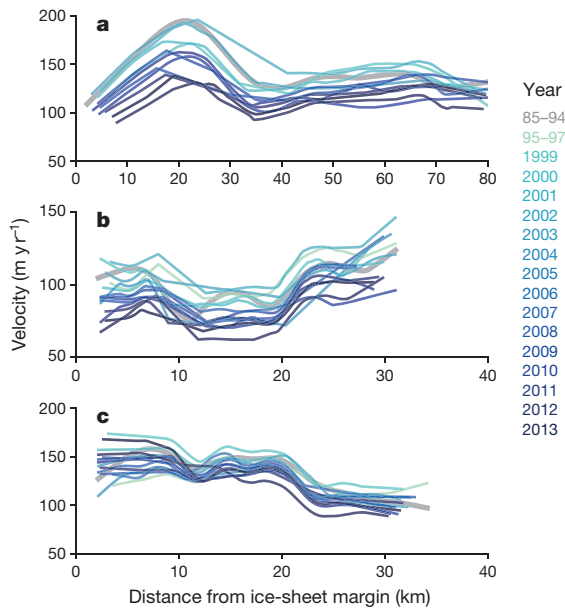


**Figure 3 | Ice velocities along three transects in the study area.** Results for **a**, transect A; **b**, transect B; **c**, transect C. These transects are shown in Fig. 1. Only periods in which ice velocities are observed along at least 60% of each transect are shown. Velocities during the 1985–94 reference period are also shown.

the GIS show that during the melt season, the large cumulative increase in the rate of meltwater supply to the ice-sheet bed results in the expansion of a channelized subglacial drainage system<sup>16</sup>, even beneath ice that is around 1 km thick<sup>11</sup>. As air temperatures warm, more meltwater at higher elevations allows an efficient drainage system to evolve, which extends further into the ice sheet. Summers of extreme melt result in a higher-capacity, more-extensive channelized drainage system, which therefore stays open at atmospheric pressure for longer after the melt ceases<sup>2,3</sup>. Dye tracing of alpine glaciers<sup>28</sup> indicates that water transit speeds through unchannelized drainage systems are  $\sim 0.01 \text{ m s}^{-1}$  ( $\sim 850 \text{ m d}^{-1}$ ). Thus, while channels at atmospheric pressure beneath ice that is about 1 km thick close within hours to days<sup>11</sup>, channels that stay open for longer, for example for just two days as opposed to one, have the capacity to evacuate notably more water from surrounding linked but unchannelized regions of the ice-sheet bed, causing more widespread dewatering of the ice–bed interface. Sources of meltwater, including frictional melting by basal slip and geothermal heat, will enable the water pressure to recover gradually through the subsequent winter, but may be insufficient to replace the stored waters evacuated during the previous melt season.

Previous observations have illustrated the importance of changes in the connectivity between channelized and unchannelized regions of the ice-sheet bed in controlling ice velocities late in the melt season<sup>12</sup>. We postulate that unchannelized drainage regions and their connectivity to the channelized drainage system govern ice motion not only late in the melt season, but also during the following winter and spring. We suggest that, if increases in drainage efficiency occur year-on-year, gradual net drainage of water stored in unchannelized regions of the ice-sheet bed will result in reduced basal lubrication and net ice slowdown. Additional field observations—such as borehole arrays, transverse to subglacial channels, recording water pressure gradients (see, for example, ref. 29), together with hydrological modelling (see, for example, ref. 14)—are required to test the robustness of our hypothesis. Furthermore, while melt-driven seasonal evolution in subglacial drainage can affect the flow of tidewater glaciers<sup>9</sup>, the ongoing acceleration of these glaciers<sup>5</sup> during a period of warming, in contrast to our observations, suggests that other processes are controlling their dynamics.

Our observations of GIS ice motion from three decades provide conclusive evidence that a 50% rise in meltwater production has not led to ice speed-up along a land-terminating margin; instead, average annual ice motion slowed by more than 15% at elevations below 800 m.a.s.l., and probably by at least 5% at elevations up to 1,100 m.a.s.l. Only about 17–33% of the slowdown can be explained by reduced internal deformation caused by ice thinning, and we therefore propose that, since 2002, increases in subglacial drainage efficiency associated with sustained larger melt volumes have reduced basal lubrication, resulting in slower ice flow. It remains unclear whether the observed slowdown occurs at elevations above 1,100 m.a.s.l., and whether the slowdown will migrate inland as enhanced melting extends to higher elevations and allows a more extensive efficient subglacial drainage system to evolve. Furthermore, our findings relate to land-terminating margins, but the forcing mechanisms that have driven the recent speed-up of many tidewater glaciers remain poorly understood<sup>5,26</sup> and require a similar examination of annual ice motion over decadal timescales.

**Online Content** Methods, along with any additional Extended Data display items and Source Data, are available in the online version of the paper; references unique to these sections appear only in the online paper.

Received 2 April; accepted 1 September 2015.

- Zwally, H. J., Abdalati, W. & Herring, T. Surface melt-induced acceleration of Greenland ice-sheet flow. *Science* **297**, 218–222 (2002).
- Sole, A. *et al.* Winter motion mediates dynamic response of the Greenland ice sheet to warmer summers. *Geophys. Res. Lett.* **40**, 3940–3944 (2013).
- Tedstone, A. J. *et al.* Greenland ice sheet motion insensitive to exceptional meltwater forcing. *Proc. Natl Acad. Sci. USA* **110**, 19719–19724 (2013).
- Shepherd, A. *et al.* A reconciled estimate of ice-sheet mass balance. *Science* **338**, 1183–1189 (2012).
- Enderlin, E. M. *et al.* An improved mass budget for the Greenland ice sheet. *Geophys. Res. Lett.* **41**, 866–872 (2014).
- Hanna, E. *et al.* Ice sheet mass balance and climate change. *Nature* **498**, 51–59 (2013).
- Box, J. E., Yang, L., Bromwich, D. H. & Bai, L.-S. Greenland ice sheet surface air temperature variability: 1840–2007. *J. Clim.* **22**, 4029–4049 (2009).
- Fettweis, X. *et al.* Important role of the mid-tropospheric atmospheric circulation in the recent surface melt increase over the Greenland ice sheet. *Cryosphere* **7**, 241–248 (2013).
- Howat, I. M., Box, J. E., Ahn, Y., Herrington, A. & McFadden, E. M. Seasonal variability in the dynamics of marine-terminating outlet glaciers in Greenland. *J. Glaciol.* **56**, 601–613 (2010).
- Das, S. B. *et al.* Fracture propagation to the base of the Greenland Ice Sheet during supraglacial lake drainage. *Science* **320**, 778–81 (2008).
- Chandler, D. M. *et al.* Evolution of the subglacial drainage system beneath the Greenland Ice Sheet revealed by tracers. *Nature Geosci.* **6**, 195–198 (2013).
- Andrews, L. C. *et al.* Direct observations of evolving subglacial drainage beneath the Greenland ice sheet. *Nature* **514**, 80–83 (2014).
- Parizek, B. R. & Alley, R. B. Implications of increased Greenland surface melt under global-warming scenarios: ice-sheet simulations. *Quat. Sci. Rev.* **23**, 1013–1027 (2004).
- Schoof, C. Ice-sheet acceleration driven by melt supply variability. *Nature* **468**, 803–806 (2010).
- Bartholomew, I. *et al.* Seasonal variations in Greenland Ice Sheet motion: Inland extent and behaviour at higher elevations. *Earth Planet. Sci. Lett.* **307**, 271–278 (2011).
- Cowton, T. *et al.* Evolution of drainage system morphology at a land-terminating Greenland outlet glacier. *J. Geophys. Res.* **118**, 29–41 (2013).
- Röthlisberger, H. Water pressure in intra- and subglacial channels. *J. Glaciol.* **11**, 177–203 (1972).
- Hoffman, M. & Price, S. Feedbacks between coupled subglacial hydrology and glacier dynamics. *J. Geophys. Res. Earth Surf.* **119**, 414–436 (2014).
- van de Wal, R. S. W. *et al.* Large and rapid melt-induced velocity changes in the ablation zone of the Greenland ice sheet. *Science* **321**, 111–113 (2008).
- van de Wal, R. S. W. *et al.* Self-regulation of ice flow varies across the ablation area in south-west Greenland. *Cryosphere* **9**, 603–611 (2015).
- Doyle, S. H. *et al.* Persistent flow acceleration within the interior of the Greenland ice sheet. *Geophys. Res. Lett.* **41**, 899–905 (2014).
- Shannon, S. R. *et al.* Enhanced basal lubrication and the contribution of the Greenland ice sheet to future sea-level rise. *Proc. Natl Acad. Sci. USA* **110**, 14156–14161 (2013).
- Dehecq, A., Gourmelen, N. & Trounev, E. Deriving large scale glacier velocities from a complete satellite archive: application to the Pamir-Karakoram-Himalaya. *Remote Sens. Environ.* **162**, 55–66 (2015).
- Morlighem, M., Rignot, E., Mouginot, J., Seroussi, H. & Larour, E. Deeply incised submarine glacial valleys beneath the Greenland ice sheet. *Nature Geosci.* **7**, 418–422 (2014).

25. Sole, A., Payne, T., Bamber, J., Nienow, P. & Krabill, W. Testing hypotheses of the cause of peripheral thinning of the Greenland ice sheet: is land-terminating ice thinning at anomalously high rates? *Cryosphere* **2**, 205–218 (2008).
26. Pritchard, H. D., Arthern, R. J. & Vaughan, D. G. and Edwards, L. A. Extensive dynamic thinning on the margins of the Greenland and Antarctic ice sheets. *Nature* **461**, 971–975 (2009).
27. Helm, V., Humbert, A. & Miller, H. Elevation and elevation change of Greenland and Antarctica derived from CryoSat-2. *Cryosphere* **8**, 1539–1559 (2014).
28. Richards, K. *et al.* An integrated approach to modelling hydrology and water quality in glacierized catchments. *Hydrol. Processes* **10**, 479–508 (1996).
29. Hubbard, B., Sharp, M., Willis, I., Nielsen, M. & Smart, C. Borehole water-level variations and the structure of the subglacial hydrological system of Haut Glacier d'Arolla, Valais, Switzerland. *J. Glaciol.* **41**, 572–583 (1995).
30. Howat, I. M., Negrete, A. & Smith, B. E. The Greenland Ice Mapping Project (GIMP) land classification and surface elevation data sets. *Cryosphere* **8**, 1509–1518 (2014).

**Supplementary Information** is available in the online version of the paper.

**Acknowledgements** A.J.T. acknowledges UK Natural Environment Research Council (NERC) studentships NE/152830X/1 and NE/J500021/1, a Scottish Alliance for

Geoscience, Environment and Society (SAGES) Postdoctoral/Early Career Researcher Exchange (PECRE) award, and a University of Edinburgh GeoSciences Moss scholarship. N.G. acknowledges European Space Agency Dragon 3 grant 10302, the Centre National d'Etudes Spatiales Tosca CESTENG project, and a fellowship from the Centre National d'Etudes Spatiales to A.D. This work made use of the resources provided by the Edinburgh Compute and Data Facility (ECDF) (<http://www.ecdf.ed.ac.uk/>). We thank P. Huybrechts for his work on the runoff/retention model used in this study. The Landsat imagery was provided by the United States Geological Survey and the European Space Agency third party missions program.

**Author Contributions** A.J.T., P.W.N. and N.G. designed this study. A.D., N.G. and A.J.T. developed the processing chain used for feature tracking of Landsat imagery. A.J.T., A.D. and N.G. processed the Landsat imagery. A.J.T. and D.G. calculated the impact of changing ice geometry upon ice motion. E.H. processed the melt data. A.J.T., N.G. and P.W.N. analysed the results. A.J.T., P.W.N. and N.G. wrote the manuscript. All authors discussed the results and edited the manuscript.

**Author Information** Reprints and permissions information is available at [www.nature.com/reprints](http://www.nature.com/reprints). The authors declare no competing financial interests. Readers are welcome to comment on the online version of the paper. Correspondence and requests for materials should be addressed to A.J.T. ([a.j.tedstone@ed.ac.uk](mailto:a.j.tedstone@ed.ac.uk)).



## METHODS

**Remote sensing of ice motion.** We applied feature-tracking techniques to extract ice motion from Landsat Program imagery. Landsat images were obtained from the US Geological Survey (via the Earth Explorer catalogue at <http://earthexplorer.usgs.gov>) and the European Space Agency (via the Earth Observation Link catalogue at <https://earth.esa.int/web/guest/eoli>). Here we provide an outline of the processing strategy and the specific parameters that we used. A detailed description of the processing strategy is available elsewhere<sup>23</sup>. Our approach builds individual annual velocity fields from feature tracking of Landsat pairs, overlapping in time and space. These velocity fields are then combined over interannual time periods in order to increase the robustness of the velocity estimates and to enable statistical determination of uncertainties.

We used images from the Landsat 5, 7 and 8 missions; the quality and quantity of images from Landsat missions 1–3 were insufficient to permit their use. We identified 475 image pairs with temporal baselines between 352 and 400 days, acquired from April to October over the 1985–2014 study period (see Supplementary Information). The temporal baseline of ~1 year was chosen to minimize the impact of seasonal flow variability upon interannual trends in ice velocity, as we are specifically interested in long-term changes in ice motion.

To enhance the images before feature tracking, we used principal component analysis to combine the optimum spectral bands, identified during testing as bands 2 and 3 for each satellite mission. A high-pass filter (using Sobel kernels) was used to compute the intensity gradients of each image, enhancing surface features such as crevasses and reducing the impact of features related to basal topography, which by definition are temporally stable. We then used the gradients as features to be tracked. The tracking (used to extract ice displacement) was performed on matching windows of 44 pixels (1,320 m) and a grid spacing of 8 pixels (240 m), while the search window was set automatically to correspond to the maximum expected displacement over the baseline duration between the two images, based on previous velocity observations<sup>31</sup>.

The processing strategy exploits the redundancy offered by multiple, spatio-temporally overlapping pairs to remove velocity outliers efficiently and produce robust velocity fields. First, we filter low-quality velocity estimates by applying a threshold to the signal-to-noise ratio returned during the feature tracking. The threshold value was determined by examining all velocity pairs to identify the value beyond which the median absolute deviation (MAD) of stable area velocities becomes asymptotic. We use a median-based approach to minimize the impact of outliers, and because the distribution of velocity tends not to follow a normal distribution<sup>23</sup>. Next, for the period 2000–14, we group velocities into one-year time periods and for the period 1985–2000, we group velocities into two-year time periods (because there were fewer Landsat pairs available). This provides spatio-temporal redundancy in the velocity estimates at each pixel and enables us to quantify uncertainties. To produce the final velocity field for each period, we compute the median of all the available velocity estimates at each pixel. Lists of the Landsat pairs that contribute to each period are available in the Supplementary Information. Finally, we compute the  $1\sigma$  uncertainty of the velocity estimate at each pixel in each period. To do so we fit a law of the form:

$$\sigma = \frac{k \text{ MAD}}{2 N^\alpha} \quad (1)$$

where  $N$  is the number of velocities used to compute the median velocity,  $\sigma$  is the  $1\sigma$  confidence interval, and  $k$  and  $\alpha$  are the parameters to be determined.  $k$  and  $\alpha$  were determined for each time period from the velocity estimates made over stable land areas whose true value is known and equal to 0. Uncertainty of the final ice velocity of each pixel at each time period is then obtained by extrapolating this relationship to on-ice areas with the appropriate values of MAD and  $N$  for a given pixel. Considering  $N$  and MAD at the pixel level allows the surface characteristics at the location of each pixel (for example, surface conditions or variability of velocity during the time period considered) to be taken into account. Pixels with  $\sigma > 60 \text{ m yr}^{-1}$  are discarded in the subsequent analysis.

We computed the percentage change in ice velocities between 1985 and 1994, and between 2007 and 2014, at all of the pixels that are common to both periods (Fig. 1); we then computed the median percentage change, both over the whole study area and in elevation bands of 100 m a.s.l.. For each elevation band in Fig. 1b, we calculated the uncertainty of the percentage change by first estimating the uncertainty of the 1985–94 ( $e_1$ ) and 2007–14 ( $e_2$ ) velocities separately as  $\sqrt{\sum_{i=1}^N \sigma_i^2 / N}$ , and then computing  $\sqrt{e_1^2 + e_2^2}$ . Residual striping patterns in Fig. 1 are caused by lines of missing data in the Landsat 5 imagery.

To compute interannual median velocities (Fig. 2b), we discarded first periods in which less than 30% of the study area has observations. Then, the pixels common to all the retained periods (Extended Data Fig. 4) were selected so as to avoid temporal variation caused by spatial bias. For each period we calculated the med-

ian of the 8,025 temporally common pixels and the associated uncertainty  $\sigma$ , estimated as  $\sqrt{\sum_{i=1}^N \sigma_i^2 / N}$ . The altitudinal distribution of the common sampling pixels is shown in Fig. 2c.

The decision to discard periods in which less than 30% of the study area has observations is a compromise between calculating the median velocity of each period using the greatest possible number of pixels common to all periods, versus retaining the maximum possible temporal resolution. We examined the sensitivity of the ice-motion time series (Fig. 2b) to 40% and 50% thresholds. At 40%, there are 5,970 more sampling pixels in common than at 30%, but temporal resolution decreases as ice velocities observed in 2003–06 are no longer retained. The  $R^2$  of the two-trend model decreases to 0.65. The rate of slowdown during 2002–14 increases from  $1.5 \text{ m yr}^{-2}$  to  $1.9 \text{ m yr}^{-2}$  ( $P < 0.01$ ). At 50%, there are 8,397 more sampling pixels in common than at 30%. Velocities observed during the 1995–97 period are also discarded. The  $R^2$  of the two-trend model is 0.63. The rate of slowdown during 2002–14 remains the same as at 40% ( $P < 0.01$ ). There is no statistically significant trend in ice motion from 1985 to 2002 ( $P > 0.05$ ) at either of the tested thresholds. From this sensitivity analysis, we conclude that our 30% threshold case yields the highest temporal resolution and also the most conservative trend in ice motion during 2002 to 2014.

**Identification of trends in melting and ice motion.** For each time series, we test whether it can be divided into temporally distinct populations separated by break dates. We apply the Mann–Whitney–Wilcoxon (MWW) rank sum test to investigate the effect of prescribing different break dates. We chose the MWW test over the  $t$ -test as we do not know whether the data set follows a normal distribution. The test computes the probability that the populations, separated by prescribed break dates, are similar.

The melt time series (Fig. 2a) consists of several years of sustained low melt, followed by a period of rising melt and then several years of sustained higher melt. We therefore test whether the melt time series can be split into three statistically different populations, with two break dates separating the periods of sustained low, rising and sustained high melt. We find that the break-date combinations of (i) 1992 and 2001, (ii) 1993 and 2001, and (iii) 1993 and 2002 are all significant with 95% confidence (Extended Data Fig. 2). To find the best possible combination of break dates, we compute the root-mean-squared error, or residuals, of the best-fitting three-trend segmented linear regression model (Extended Data Fig. 2). We observe the lowest residuals for break dates of 1991–93 and 2001–04. The combination of break dates that satisfies the MWW test and has the lowest residuals is 1993 and 2002. With this chosen combination of break dates, the probability that (i) 1985–93 is similar to 2002–13 is 0.02%; (ii) 1985–93 is similar to 1994–2001 is 2%; and (iii) 1994–2001 is similar to 2002–13 is 3%.

For the ice-motion time series, we first test whether it can be divided into two temporally distinct populations, in order to justify the use of segmented linear regression (Fig. 2). We apply the MWW test as previously. We find that for break dates beyond mid-2001, the null hypothesis (equal median) can be rejected (Extended Data Fig. 3a), meaning that the pre- and post-2001 populations are statistically different with 95% confidence. To test the ability of two distinct periods separated by a given break date to represent the velocity time series, we then compute the residuals of the best fitting two-trend segmented linear regression model for a set of break dates spanning the time period of the data set (Extended Data Fig. 3b). We observe a minimum for a break date in 2002, but with a region of low residuals spanning the period 1998 to 2004. We conclude from these tests that there are two distinct temporal populations of ice motion in our data set and that the break point occurs during the period 1998 to 2004. For our analysis (Fig. 2) we select a break date of 2002, which corresponds both with the lowest residuals and with the MWW test that suggests that the pre- and post-2002 populations are statistically different.

We then examine whether there is a statistically significant relationship between meltwater production and ice motion by applying linear regression analysis to investigate the extent to which variability in ice motion can be explained by, first, temporally coincident, and second, antecedent meltwater production (Extended Data Table 1). We quantify antecedent meltwater production in two different ways. In one scenario we calculate the mean during the period of observed ice motion and the preceding  $N$  years. In the other scenario we calculate the mean of only the preceding  $N$  years.

**Impact of varying baseline durations on annual velocity.** Images separated by baseline durations of 352–400 days were paired together for feature tracking. Here we examine the impact that the variable baseline duration has on the velocity field of each period.

The average start dates of the pairs that comprise each period are shown in Extended Data Fig. 1a. The start day becomes less variable once imagery from Landsat 7 comes online in 1999. The average baseline duration increases by about 15 days after 1999 (Extended Data Fig. 1b), increasing the proportion of the

baseline that is attributable to summer motion (defined as 1 May to 31 August, in common with previous studies<sup>2,3</sup>) by about 2% (Extended Data Fig. 1c).

We use mean summer and winter velocities from Leverett Glacier sites S1 to S4 during the period 2009 to 2012 (refs 2, 3) to test the sensitivity of annual velocities to the varying baseline duration. Winter days in each period are ascribed velocities of  $81.6 \text{ m yr}^{-1}$  and summer days are ascribed velocities of  $127.6 \text{ m yr}^{-1}$ . We then estimate the mean annual velocity that would be expected for each period (Extended Data Fig. 1d). Variations in the baseline duration between periods are estimated to affect extracted annual ice motion by more than  $2 \text{ m yr}^{-1}$ . Furthermore, according to this analysis, increased baseline durations during the 2000s leads to a small artificial increase in ice motion caused by the feature-tracking method. This is in the opposite direction to the interannual slowdown signal that we observe in our study area, leading us to conclude that our slowdown trend is robust to varying baseline durations.

**Impact of changing ice geometry on velocity.** During the past 30 years, the GIS has thinned along its margins<sup>26,27,32</sup>, changing the geometry of the ice mass. It is likely that these changes will have affected ice velocity by modifying driving stress. Here we evaluate the impact that thinning may have had on velocity along transect A (Fig. 1), in order to bound the extent to which our observed slowdown could be the result of geometric changes.

We characterize the surface velocity  $u_s$  as the sum of a basal sliding ( $u_b$ ) and a vertical shear deformation ( $u_d$ ) contribution<sup>33</sup>:

$$u_s = u_b + u_d = C_b(\rho_i g S H)^m + \frac{A}{4}(\rho_i g S)^3 H^4 \quad (2)$$

where  $A$  is a temperature-dependent Glen's flow parameter,  $\rho_i$  is the density of ice,  $g$  is gravitational acceleration,  $S$  is the surface slope (positive where the surface lowers towards the margin),  $H$  is the ice thickness, and  $C_b$  and  $m$  are parameters related to basal sliding.  $A$ ,  $C_b$  and  $m$  are in general poorly constrained, and are likely to vary spatially; however, the only assumptions we make in our analysis regarding these parameters are that they do not change markedly over the time interval of interest, and that  $m$  is less than or equal to 3. Note that our model allows for either the power-law rheological model of Weertman<sup>34</sup> or the Newtonian till model of Alley *et al.*<sup>35</sup>. Thus the maximum deceleration predicted by the above model bounds the slowdown that can be explained by geometric changes alone. Below, we estimate this maximum deceleration to first order.

We introduce the variable  $\lambda$ , which represents the fraction of surface velocity that can be explained by vertical shear, that is,  $u_d = \lambda u_s$ ,  $u_b = (1 - \lambda)u_s$ .

If we consider a small change  $\delta S$  in slope ( $\delta S \ll S$ ), and a small change  $\delta H$  in ice thickness ( $\delta H \ll H$ ), equation (2) leads to the following change in  $u_s$ :

$$\begin{aligned} \delta u_s &= \left( \frac{m u_b + 3 u_d}{u_s} \right) \frac{\delta S}{S} + \left( \frac{m u_b + 4 u_d}{u_s} \right) \frac{\delta H}{H} + \theta(\delta H^2, \delta S^2) \\ &= (m(1 - \lambda) + 3\lambda) \frac{\delta S}{S} + (m(1 - \lambda) + 4\lambda) \frac{\delta H}{H} + \theta(\delta H^2, \delta S^2) \end{aligned} \quad (3)$$

where the  $\theta$ -notation is used to signify terms that are of order  $\delta H^2$  and  $\delta S^2$  or higher and thus are negligibly small. Again, we make no assumption regarding the spatial variability of  $\lambda$ , other than that it is between 0 and 1, as our aim is to find the

conditions under which velocity is most sensitive to thinning. With  $\left( \frac{\delta S}{S} \right)$  positive

and  $\left( \frac{\delta H}{H} \right)$  negative in equation (3), then at any point along the transect, and for any  $m \leq 3$ , the change to  $u_s$  cannot be more negative than when the flow is due to vertical shear, that is, when  $\lambda$  is equal to 1. The first-order relative change in surface velocity,  $\frac{\delta u_s}{u_s}$ , is thus bounded by:

$$3 \frac{\delta S}{S} + 4 \frac{\delta H}{H} \quad (4)$$

We use equation (4) to estimate the maximal impact of these thinning scenarios on ice velocity, solving every 240 m along transect A. To estimate the total ice thinning during 1985–2014,  $\delta H = 10, 20$  are prescribed at the ice-sheet margin and linearly

interpolated along the transect to  $\delta H = 0 \text{ m}$  at 100 km inland (equivalent to the equilibrium line altitude,  $\sim 1,500 \text{ m a.s.l.}$ , ref. 36) (Extended Data Fig. 5a). We add  $\delta H$  to current ice thickness along the transect<sup>24</sup> to set  $H$  to values appropriate for 1985. We prescribe the initial slope  $S$  as the mean slope in our study area,  $0.02 \text{ m m}^{-1}$ . The change in slope,  $\delta S$ , is calculated from the prescribed linear change in ice thickness over distance inland.

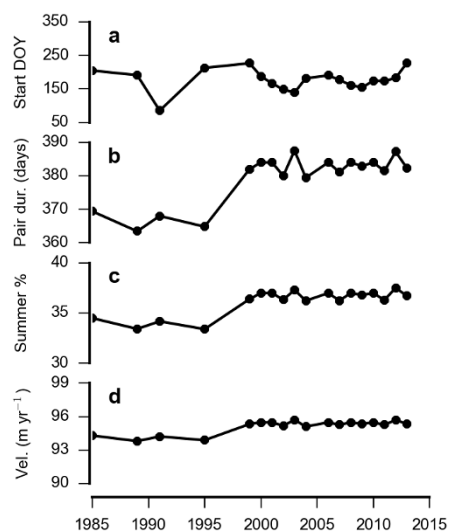
In Extended Data Fig. 5b we plot equation (4) according to the two thinning scenarios described above. These profiles represent the largest (that is, the most negative) percentage changes in velocity associated with the prescribed geometric change. We then convert these profiles to the predicted reductions in velocity and remove them from the observed 1985–94 velocities (Extended Data Fig. 5c), generating a lower bound for the 2007–14 velocities under the assumption that the observed slowdown was geometrically induced. Between about 0 km and 5 km from the ice margin for the  $\delta H = 20 \text{ m}$  scenario, the observed slowdown is within the range predicted by equation (4), and we cannot reject the possibility that the thinning here was responsible for the slowdown. However, between 10–50 km inland, at most 17–33% of the observed slowdown can be attributed to changing ice-sheet geometry depending on the prescribed  $\delta H$ . By 60 km inland, there is essentially no net change in ice velocity attributable to geometrical changes.

Finally we must consider our assumption that the Glen's law parameter  $A$  can be treated as constant in time. Phillips *et al.*<sup>37</sup> showed that latent heat transferred to the ice from surface melt could warm glacial ice at depth, thereby leading to an increase in  $A$ . However, this process would result in acceleration rather than deceleration. Thus our decision not to consider temporal changes in  $A$  in our analysis of maximal geometrically induced slowdown is justified. We conclude that the slowdown that we have observed during 1985–2014 is not explicable by geometrical changes to the ice sheet alone, and instead must be dominated, at distances greater than  $\sim 5 \text{ km}$  from the margin, by other processes that affect basal motion.

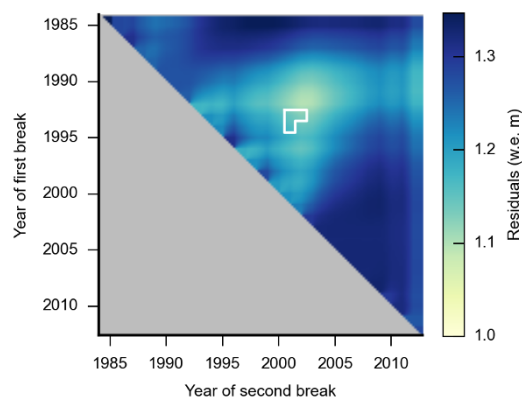
**Surface melting.** GIS annual melting was output from a runoff/retention model applied to downscaled ERA-interim data from the European Centre for Medium-Range Weather Forecasts (ECMWF) on an equal-area  $5 \text{ km} \times 5 \text{ km}$  polar stereographic grid for the Greenland region<sup>38</sup>. We calculated mean annual melt rates for the study area ( $67.45^\circ \text{ N}$ ,  $51.5^\circ \text{ W}$  to  $69.2^\circ \text{ N}$ ,  $49.2^\circ \text{ W}$ ). Interannual fluctuations and trends from several independent melt models show good agreement<sup>39</sup>, including with the methodology used in this study.

**Code availability.** The feature-tracking algorithm is proprietary software developed and licensed by GAMMA Remote Sensing. Requests for the code underlying the processing strategy used here should be sent to the original authors<sup>23</sup>. Similarly, requests for the code constituting the runoff/retention model should be addressed to its original authors<sup>40</sup>.

31. Joughin, I., Smith, B. E., Howat, I. M., Scambos, T. & Moon, T. Greenland flow variability from ice-sheet-wide velocity mapping. *J. Glaciol.* **56**, 415–430 (2010).
32. Krabill, W. *et al.* Greenland ice sheet: high-elevation balance and peripheral thinning. *Science* **289**, 428–430 (2000).
33. Cuffey, K. & Paterson, W. S. B. *The Physics of Glaciers* 3rd edn (Butterworth-Heinemann, 2010).
34. Weertman, J. On the sliding of glaciers. *J. Glaciol.* **3**, 33–38 (1957).
35. Alley, R. B., Blankenship, D. D., Rooney, S. T. & Bentley, C. R. Till beneath ice stream B: 4. A coupled ice-till flow model. *J. Geophys. Res. Solid Earth* **92**, 8931–8940 (1987).
36. van de Wal, R. S. W. *et al.* Twenty-one years of mass balance observations along the K-transect, West Greenland. *Earth Syst. Sci. Data* **4**, 31–35 (2012).
37. Phillips, T., Rajaram, H. & Steffen, K. Cryo-hydrologic warming: a potential mechanism for rapid thermal response of ice sheets. *Geophys. Res. Lett.* **37**, L20503 (2010).
38. Hanna, E. *et al.* Greenland ice sheet surface mass balance 1870 to 2010 based on twentieth century reanalysis, and links with global climate forcing. *J. Geophys. Res.* **116**, D24121 (2011).
39. Vernon, C. L. *et al.* Surface mass balance model intercomparison for the Greenland ice sheet. *Cryosphere* **7**, 599–614 (2013).
40. Janssens, I. and Huybrechts, P. The treatment of meltwater retention in mass-balance parameterizations of the Greenland ice sheet. *Ann. Glaciol.* **31**, 133–140 (2000).

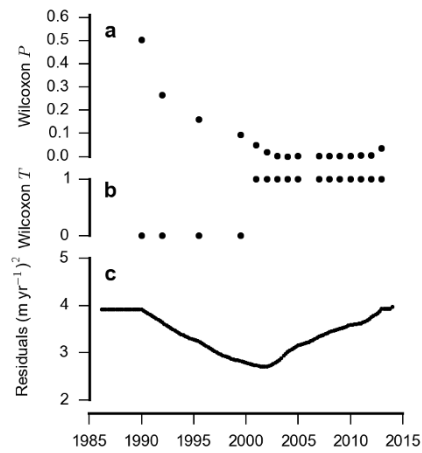


**Extended Data Figure 1 | Sensitivity of extracted ice motion to variations in baseline duration.** For each period are shown: **a**, the average start day-of-year (DOY) of all pairs used in the period; **b**, the average baseline duration of all pairs used in the period; **c**, the proportion of the baseline duration that is attributable to summer, which is defined as 1 May to 31 August; and **d**, the annual velocity that would be expected in the ablation zone of the Leverett glacier catchment, based on the average proportion of summer versus winter and the average baseline duration for each year.

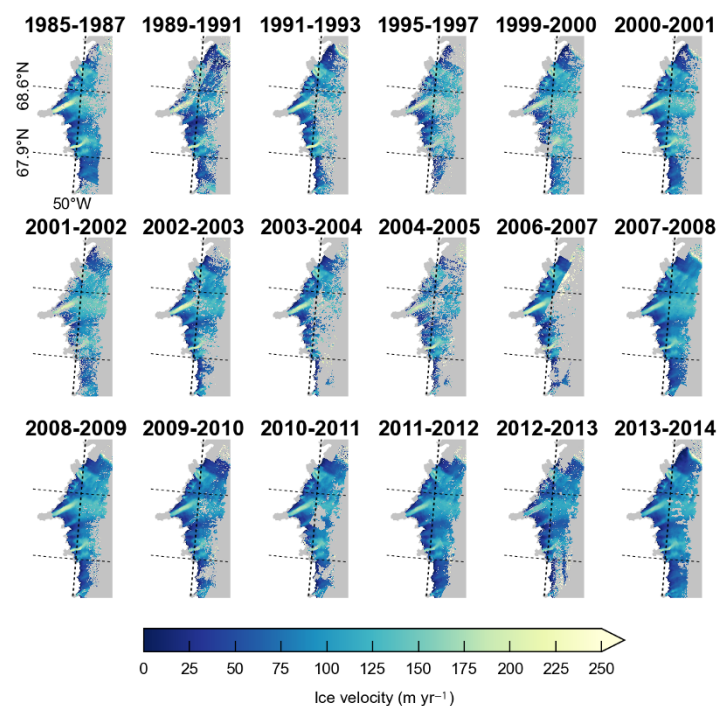


**Extended Data Figure 2 | Statistical significance of three different periods of surface meltwater production.** Hypothesis test of the Wilcoxon rank sum test at 95% confidence (see Methods), showing that three periods of surface melt separated by the specified dates have statistically different medians (outlined white region). The colouring shows the residuals of a three-trend linear segmented regression model fitted to melting at each possible combination of two break dates, expressed as the root-mean-squared error. The grey area is shaded as such for simplicity; it would otherwise be a mirror image of the coloured area.

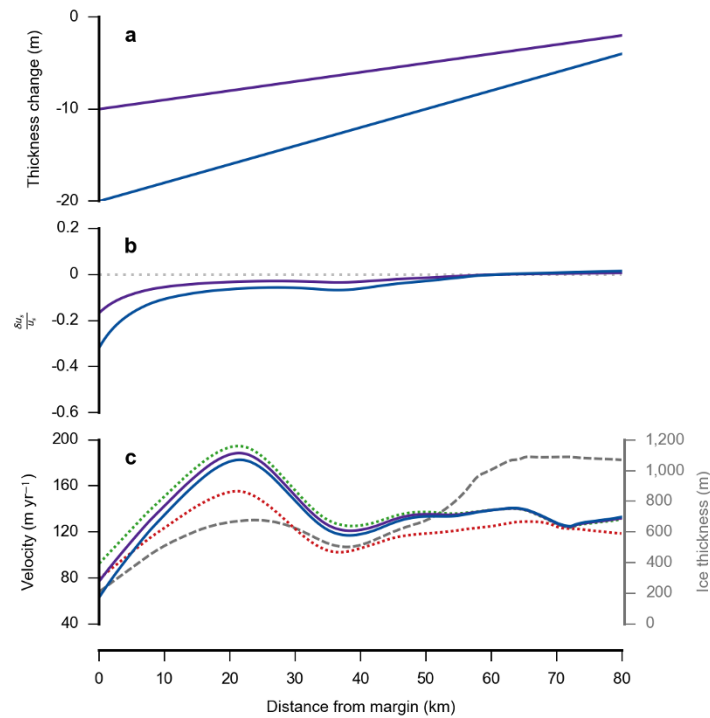




**Extended Data Figure 3 | Statistical significance of two different periods of ice motion.** **a**, Hypothesis test of the Wilcoxon rank sum test for equal medians, testing the probability that the two populations (separated by the specified date) are similar, with 95% confidence. 0 signifies that the hypothesis of equal medians cannot be rejected, and 1 signifies that the hypothesis of equal medians can be rejected. **b**, Residuals shown as the sum-of-squares  $(\text{m yr}^{-1})^2$  of a two-trend model fitted to velocities at each possible break date.



**Extended Data Figure 4 | Ice velocities during each period.** The velocities have uncertainties  $< 60 \text{ m yr}^{-1}$  and were observed across at least 30% of the study area in each period (see Methods).



**Extended Data Figure 5 | Impact of changing ice geometry on ice motion.** Ice thinning of 10 m (purple) and 20 m (blue) at the ice margin, through to 0 m at 100 km inland, was applied to transect A. **a**, Prescribed change in ice thickness over transect length. **b**, The ratio of velocity change, calculated from

equation (4). **c**, Left axis, observed ice velocity during 1985–94 (dotted green) and 2007–14 (dotted red). Modelled velocities in 2014 (solid lines) for the prescribed ice thicknesses. Right axis, ice thickness (dashed grey)<sup>24</sup>.

Extended Data Table 1 | Statistical relationship between melting and ice motion

Years preceding period ( $N$ )	Period and preceding $N$ years		Preceding $N$ years only	
	$R^2$	$p$	$R^2$	$p$
0	0.08 <sup>(1)</sup>	0.23	-	-
1	0.23	0.04	0.28	0.02
2	0.35	< 0.01	0.48	< 0.01
3	0.41	< 0.01	0.50	< 0.01
4	0.44	< 0.01	0.50	< 0.01

The results of linear regression analysis carried out between all periods of ice motion in Fig. 2b and different estimates of temporally coincident<sup>(1)</sup> and antecedent meltwater production (see Methods).